International Journal of Nanomedicine

Dovepress
Taylor & Francis Group

Open Access Full Text Article

ORIGINAL RESEARCH

Near-Infrared Light-Responsive Copper Selenide Nanoparticle-Loaded Calcium Silicate Cement Induces Immunogenic Cell Death in Osteosarcoma

Ruitang Liu[1,2,*], Ruilong Sun[1,*], Yun Xue[1,*], Yigui Zhou[1], Longwen Zhan[1], Yunfei Li[1], Yongzheng Tian[1], Chunyang Wang[1], Weike Feng[1], Bin Chang[1], Bo Fan[1], Qiuming Gao[1]

[1]Orthopedic Center, The 940th Hospital of the Joint Logistic Support Force of Chinese People's Liberation Army, Lanzhou, People's Republic of China; [2]Gansu Provincial Key Laboratory of Stem Cells and Gene Drugs, Lanzhou, People's Republic of China

*These authors contributed equally to this work

Correspondence: Bo Fan; Qiuming Gao, Email fanbo1228@163.com; gaoqm001@sohu.com

Introduction: Osteosarcoma is a highly malignant tumor posing significant treatment challenges, including limited efficacy of conventional therapies and difficulties in bone defect repair following resection. Although calcium silicate cement (CS) exhibits favorable characteristics as a bone filler, such as moldability and high compressive strength, its inherent lack of antitumor properties restricts its use in oncological contexts.

Methods: A multifunctional composite bone cement was developed by incorporating nano-Cu2-xSe—a photothermal agent synthesized via a one-pot method—into a CS matrix. The material was systematically evaluated in terms of photothermal performance, setting time, compressive strength, and antitumor efficacy through in vitro assays and in vivo experiments using animal models. Mechanistic studies were conducted to assess whether immunogenic cell death (ICD) was induced in tumor cells.

Results: The addition of only 0.2 wt% nano-$Cu_{2-x}Se$ enabled effective photothermal conversion under near-infrared (NIR) irradiation, reaching temperatures necessary for photothermal therapy (PTT). The composite cement also exhibited a shorter setting time and higher compressive strength compared to pure CS. Both in vitro and in vivo tests confirmed its potent antitumor efficacy, with mechanistic analysis revealing the induction of ICD in tumor cells.

Discussion: This composite cement constitutes a dual-functional system capable of supporting bone defect repair while providing a photothermal antitumor effect, with potential immunogenic properties. The combination of improved material properties and efficient PTT performance highlights its promise as a strategy for treating bone tumors in a preclinical setting. These results support further development of this material for future translational studies in bone tissue engineering and oncology.

Keywords: nano particle, photothermal therapy, calcium silicate, osteosarcoma, immunogenic cell death

Introduction

Osteosarcoma, a primary malignant tumor originating from bone marrow mesenchymal stem cells (BMSCs),[1] predominantly affects adolescents and manifests clinically as bone pain, hypercalcemia, and pathological fractures.[2–5] Characterized by high invasiveness and metastatic potential, this malignancy leads to poor prognosis and low survival rates.[6,7] Current treatment strategies combining surgery with chemotherapy face significant limitations: residual tumor cells frequently induce recurrence and metastasis prior to chemotherapy initiation, while chemoresistance and systemic toxicity further compromise therapeutic efficacy.[8] The critical challenge lies in achieving precise tumor eradication while simultaneously restoring bone mechanical integrity to enhance patient survival outcomes.[9,10]

Received: 21 June 2025
Accepted: 22 October 2025
Published: 11 November 2025

For post-surgical bone defect reconstruction, conventional approaches using autografts, allografts, and synthetic bone substitutes present notable drawbacks. Autografts are constrained by donor site morbidity and limited availability,[11] allografts carry risks of disease transmission and immune rejection,[12] while synthetic alternatives face cost-related accessibility barriers.[13] Calcium-based bone cements emerge as promising alternatives due to their biocompatibility, mechanical compatibility, and cost-effectiveness.[14–16] Among current formulations: Calcium sulfate demonstrates mismatched degradation kinetics relative to bone regeneration rates and poor osseointegration despite historical usage;[17] Calcium phosphate, though compositionally similar to natural bone, suffers from prolonged setting times and inadequate mechanical stability;[18] Calcium silicate(CS) distinguishes itself through superior self-setting properties and bioactivity, with released calcium/silicon ions activating osteogenic gene expression to promote bone regeneration.[19,20] However, conventional cements lack inherent antitumor functionality, necessitating systemic chemotherapy. This drives research interest in developing smart bone cements integrating both antitumor and osteoregenerative capabilities.

Drug-loaded bone cements enable localized tumor therapy through three primary modalities: (1) Chemo/radiotherapeutic systems minimize systemic toxicity but risk material instability and peri-implant tissue damage during prolonged drug release;[21–24] (2) Magnetothermal cements require high-power alternating magnetic fields for thermal ablation, posing risks of cutaneous burns;[25] (3) Photothermal systems use the deep penetration ability of near infrared light (NIR) to trigger the heat generation of photothermal agents, which can achieve efficient tumor ablation at low power (<1W) with little damage to the surrounding normal tissues.[26–30] However, the clinical translation of many conventional photothermal agents is often hampered by their potential long-term toxicity concerns, such as the hepatic toxicity associated with copper-based nanomaterials like $Cu_{2-x}S$, or the biosafety debates surrounding certain inorganic nanoparticles.[31] Additionally, some organic agents, despite their high phototoxic indices, may still face challenges related to photostability and reproducibility in the complex biological environment of bone tissue.[32] These limitations underscore the pressing need for developing novel photothermal agents that combine high biocompatibility with potent and reliable photothermal performance. To address these issues, copper selenide (CuSe) has emerged as a promising alternative due to its reportedly lower toxicity and excellent photothermal conversion efficiency.[33]

$Cu_{2-x}Se$ nanoparticles have emerged as exceptional photothermal agents in oncology. Zhang et al[34] synthesized $Cu_{2-x}Se$ nanoparticles demonstrating dual enzyme-mimetic activities (peroxidase-like and glutathione oxidase-like) alongside remarkable photothermal conversion efficiency. The elevated glutathione (GSH) concentration in the tumor microenvironment (approximately 10-fold higher than in normal cells) confers enhanced antioxidant capacity to tumor cells, enabling them to counteract reactive oxygen species (ROS)-mediated damage.[35–37] $Cu_{2-x}Se$ nanoparticles counteract this protective mechanism through their dual enzymatic activities, effectively reducing tumor cell resistance to oxidative stress and thereby establishing a therapeutic foundation for photothermal tumor ablation. Furthermore, $Cu_{2-x}Se$ nanoparticles exhibit immunomodulatory properties that address critical limitations in anti-tumor immunity. Malignant tumors frequently demonstrate post-surgical recurrence and distant metastasis, primarily due to insufficient T lymphocyte infiltration, low tumor-associated antigen presentation, and diminished Major Histocompatibility Complex class I (MHC I) expression - factors that impair CD8+ T cell activation and cytotoxic function.[38–42] Notably, Li et al[43] demonstrated that $Cu_{2-x}Se$ nanoparticles induce Imunogenic cell death(ICD) in tumor cells, resulting in increased membrane exposure of tumor-associated antigens. Through their Fenton-like catalytic activity, these nanoparticles facilitate antigen lysosomal escape in dendritic cells (DCs), thereby enhancing MHC I-mediated antigen presentation. This cascade effect promotes the proliferation and differentiation of naive T cells into tumor-specific CD8+ cytotoxic T lymphocytes while simultaneously increasing the proportion of memory T cells in murine splenic tissue. These combined immunostimulatory effects contribute to long-term anti-tumor immunity and reduced recurrence potential.

Herefore, this study proposes to develop a novel anti-tumor CS-$Cu_{2-x}Se$ cement through the integration of photothermal $Cu_{2-x}Se$ nanoparticles synthesized via a one-pot method[44] into CS. The optimized formulation will be systematically selected by evaluating key performance parameters including photothermal conversion efficiency, setting time, compressive strength, porosity, and degradation rate under NIR irradiation. Comprehensive biological assessments will be conducted to characterize the material's cytotoxicity, NIR-responsive tumor ablation efficacy against osteosarcoma in both in vitro and in vivo models, and associated immune response mechanisms (Scheme 1). This investigation aims to establish a scientific foundation for advancing photothermal ablation-based bone cement

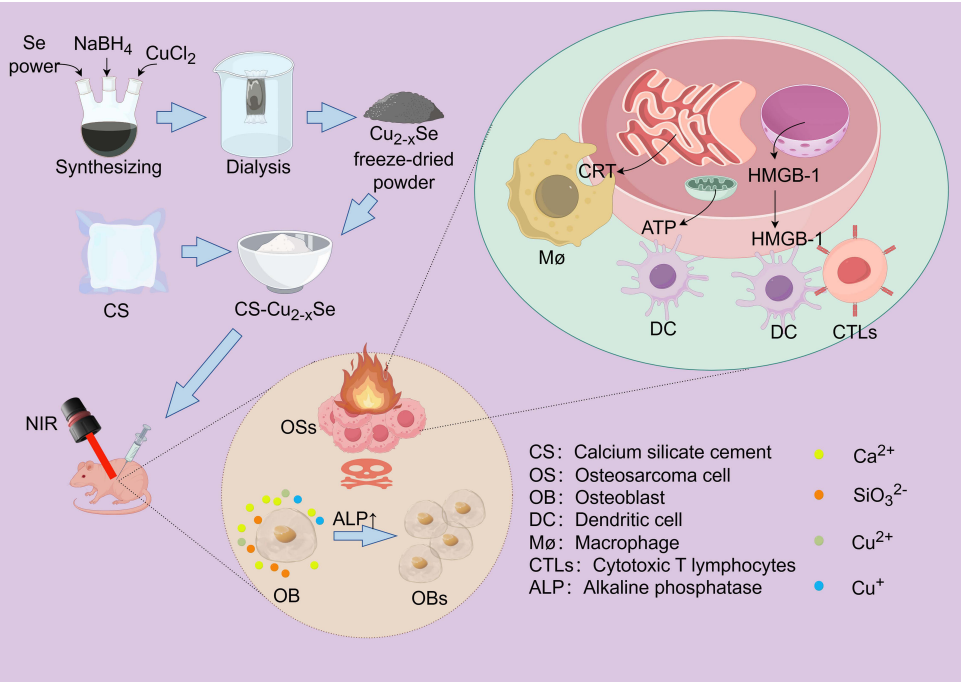

Scheme 1 Preparation Process of CS-Cu2-xSe and Its Dual Mechanisms for Osteosarcoma Cell Elimination and Osteogenic Promotion in In Vivo Studies. By Figdraw.

platforms in osteosarcoma treatment through dual optimization of material properties and immunomodulatory functionality.

Materials and Methods

Materials

Anhydrous copper chloride ($CuCl_2$, 98%, Wujiang Runtai Fine Chemical Co., LTD).; Selenium powder (Se, 99.99%, Sichuan Fu New Material Technology Co., LTD).; Dialysis bag (molecular rejection 100000 D, YTKH life sciences, USA); Sodium borohydride ($NaBH_4$, AR, Huainan Wanqi Chemical Technology Co., LTD).; Tricalcium silicate (Ca_3SiO_5, 12168–85-3, Hubei Xinyuhong Biomedical Technology Co., LTD).; Polyvinylpyrrolidone (PVP, average molecular weight 55000, Jinan Jibin Chemical Co., LTD).; Polyethylene tetrofluoride mold (6*12mm, 10*2mm, Wuhan Youdao Zhijian Biotechnology Co., LTD)., the water used in this experiment was deionized water (18.2MΩ). CCK-8 reagent (AR1160, BOSTER); Alkaline phosphatase detection kit (RXFG0127-48, Ruixin Biology); ATP assay kit (A095-1-1, Nanjing Jiancheng Biological Research Institute); Phosphate buffer solution (BL302A, Biosharp); Antibody to CTR (FNab01224, FineTest); anti-HMGB1 antibody (FNab10710, FineTest); DAPI (BL105A, Biosharp). All the mice used in this experiment were SPF nude mice (14–16g, male) purchased from Lanzhou Veterinary Research Institute, Chinese Academy of Agricultural Sciences. All animal care and experimental procedures were conducted in accordance with the "Rules and Guidelines for Animal Management of the Ministry of Health, People's Republic of China" and approved by the Scientific Research Management Ethics Committee of the 940th Hospital of the Joint Logistic Support Force of the Chinese people's Liberation Army, with ethics approval number 2024KYLL033.

Microplate reader (iMark, Bio Rad, USA); Inverted microscope (RCX41, Shun Yu, Ningbo); Ultra micro ultraviolet spectrophotometer (Aurora-900, Shanghai Chengke); Inductively Coupled Plasma Mass Spectromete (ICP-MS, Agilent-7900, USA); Incubator (DNP-9022, incubator); Embedding machine (HistoCore Arcadia, LEICA, Germany); Microtome (RM2016, LEICA, Germany); Panoramic slice scanner (Pannoramic MIDI II, Jinan Tangier Electronics Co., LTD).; Microscope (DX50, Sunny Optical Technology Co., LTD).

https://doi.org/10.2147/IJN.S548764

Synthesis of $Cu_{2-x}Se$ Nanoparticles

The synthesis commenced with thorough cleaning of glassware, including a three-necked flask, splash guard, and gas inlet tube, using deionized water. Selenium powder (39.48 mg) was precisely weighed and transferred into the three-necked flask containing 50 mL deionized water. The sealed system underwent magnetic agitation at 200 rpm for 30 min under nitrogen filled condition. Subsequently, a freshly prepared sodium borohydride solution (56.75 mg $NaBH_4$ in 2 mL deionized water) was injected into the reaction system via syringe, followed by vigorous stirring at 700 rpm for 150 min. Following solution clarification, copper(II) chloride (134 mg) and polyvinylpyrrolidone (40 mg) dissolved in 2 mL deionized water through ultrasonication were introduced into the mixture. The reaction proceeded at 1200 rpm for 90 min under continuous nitrogen flow. The resultant colloidal solution underwent purification via dialysis (MWCO 3.5 kDa) against deionized water for 48 h. Finally, the purified $Cu_{2-x}Se$ dispersion was pre-frozen at −80°C and lyophilized using a vacuum freeze-dryer. The obtained nanoparticles were stored at −20°C for subsequent characterization and application.

Preparation of CS-$Cu_{2-x}Se$ Cement

A series of $Cu_{2-x}Se$ solutions (0.2, 1, 2, 4, and 8 mg/mL) were prepared in 10 mL centrifuge tubes by ultrasonication (12 min) with deionized water. CS powder was subsequently mixed with either deionized water or the prepared $Cu_{2-x}Se$ solutions at a constant liquid-to-powder ratio of 0.5 mL/g, yielding six distinct cement formulations: pure CS cement (control) and CS-$Cu_{2-x}Se$ composites with mass ratios of 0.01 wt%, 0.05 wt%, 0.1 wt%, 0.2 wt%, and 0.4 wt% (designated as CS, CS-1$Cu_{2-x}Se$, CS-5$Cu_{2-x}Se$, CS-10$Cu_{2-x}Se$, CS-20$Cu_{2-x}Se$, and CS-40$Cu_{2-x}Se$, respectively). The cement pastes were cast into polytetrafluoroethylene molds with defined geometries - cylindrical (6 mm diameter × 12 mm height) and disc-shaped (10 mm diameter × 2 mm thickness). Specimens underwent sequential curing under controlled conditions: primary setting at 37°C with saturated humidity for 5 h followed by demolding, then secondary curing under identical environmental parameters until reaching 24 h maturation. This protocol generated dimensionally standardized cement samples for subsequent physicochemical and biological evaluations.

Characterization of $Cu_{2-x}Se$ Nanoparticles

Morphological Analysis

Transmission electron microscopy (TEM) was employed to characterize the nanostructure of $Cu_{2-x}Se$ particles. Specimens were prepared by dispersing the nanoparticles in deionized water via ultrasonication, followed by deposition onto ultrathin carbon-coated copper grids (300 mesh). Excess suspension was removed by gentle blotting with filter paper prior to TEM observation at 200 kV accelerating voltage.

Compositional and Structural Characterization

X-ray photoelectron spectroscopy (XPS) analysis was conducted using monochromatic Al Kα radiation (1486.6 eV), with powdered samples adhered to conductive carbon tape for charge neutralization. High-resolution spectra were acquired to determine elemental composition and chemical valence states. Phase identification was performed via X-ray diffraction (XRD) using Cu Kα radiation (λ = 1.5406 Å) over a 2θ range of 10°-90° with a step size of 0.02°. Rietveld refinement of XRD patterns enabled crystallographic structure verification.

Characterization of CS-$Cu_{2-x}Se$ Bone Cement

Composition and Crystallinity Analysis

The hydrated cement (CS, CS-1/5/10/20/40$Cu_{2-x}Se$) were crushed into test pieces and analyzed by XRD at 0° to 90°. To investigate the effects of different concentrations of $Cu_{2-x}Se$ on $Ca(OH)_2$ crystal phase and crystallinity of CS bone cement after hydration.

Microstructure Observation

After hydration, the column cement samples (CS, CS-1/5/10/20/40$Cu_{2-x}Se$) were freeze-dried in a vacuum freeze dryer for 72 hours to complete constant cement weight. The cement sections of each component were subsequently scanned and analyzed using a ZEISS-GeminiSEM500 scanning electron microscope. The morphology of different components of

cement and the needle-like structure of C-S-H were observed to explore the effects of different concentrations of $Cu_{2-x}Se$ on the morphology of CS cement and C-S-H after hydration product.

Photothermal Properties

Firstly, the photothermal properties of the cement paste were tested. The vertical height of the infrared laser from the sample surface was adjusted to 10cm, and a circular light spot with a diameter of 1 cm was irradiated on the sample surface. The current of the near-infrared light emission laser is set to 0.83A, and the corresponding power is 700mw according to the instructions. According to S (circular spot) =0.785 cm^2, the power density can be known to be 891mW·cm^{-2}. The temperature recorded before the irradiation of the infrared laser is taken as the initial horizontal line temperature. Due to the poor thermal conductivity of polyethylene tetrafluoride molds, heat accumulation is prone to cause temperature rise. To this end, we designed and 3D printed aluminum molds with better heat dissipation. The cement pasts (CS, CS-1/5/10/20/40$Cu_{2-x}Se$) were placed in disc-shaped aluminum molds with a diameter * height of 10*2mm. A sealed bag is placed on the mold jacket to prevent the temperature from being affected by the evaporation of water from the cement paste when the infrared laser is irradiated. The irradiation time of infrared thermal imager was 10min, and the temperature change was recorded every 50s. Six samples were collected from each group and the average value was taken.

Cement disks (CS, CS-1/5/10/20/40$Cu_{2-x}Se$) were placed on tiled aluminum foil and irradiated with an infrared laser for 10min and recorded once at 50s intervals. Finally, the photothermal data of the hydrated cement were recorded. Six samples were collected from each group and the average value was taken.

Furthermore, we also referred to Wang's method[45] and measured to calculate the photothermal conversion efficiency of copper selenide. The photothermal conversion efficiency (η) of the $Cu_{2-x}Se$ nanoparticles was determined using the following equation:

$$\eta = \frac{hS(T_{max} - T_{surr}) - Q_{dis}}{I\left(1 - 10^{-A808}\right)}$$

In this equation, h denotes the heat transfer coefficient, S is the surface area of the container, T_{max} represents the equilibrium temperature, T_{surr} is the ambient temperature, Q_{dis} signifies the heat dissipation attributed to the light absorption by the pure solvent (measured as 17.0 mW in this work, and the heat dissipation coefficient is calculated as 0.6W/(m·K)), I is the incident laser power (891 mW·cm^{-2}), and A_{808} is the absorbance of the $Cu_{2-x}Se$ solution (4 mg/mL) at the 808 nm irradiation wavelength, as obtained from the UV-Vis-NIR absorption spectrum. The product of the heat transfer coefficient and surface area (hS) was derived from the cooling phase subsequent to the cessation of irradiation, according to the equation:

$$hS = \frac{cm}{\tau_s}$$

Here, c and m are the specific heat capacity of water (4.2 J·g^{-1}·°C^{-1}) and the mass of the aqueous sample (1.0 g), respectively. The system time constant (τ_s) was determined by fitting the linear plot of the cooling time (t) against the negative natural logarithm of the driving force temperature, as defined by the equation:

$$t = -\tau_s \ln\theta = -\tau_s \ln\left(\frac{T - T_{\text{surr}}}{T_{\max} - T_{\text{surr}}}\right)$$

Setting Time

Cement pastes (CS, CS-1/5/10/20/40$Cu_{2-x}Se$) were respectively filled into the test dish and cured in a constant temperature and humidity box (37°C, 100% humidity), and measured once every 30 minutes. It was measured every 5min near final setting. The final setting time is determined when the annular attachment of the Vicat apparatus ceases to produce a visible indentation on the cement paste surface, measured in accordance with ASTM C191 standard protocols.

 https://doi.org/10.2147/IJN.S548764

To ensure accuracy, an immediate retest is required, and final setting state can be confirmed only when the results of three consecutive measurements are consistent. Six samples were collected from each group and the average value was taken.

Test the setting time of cement paste under NIR. Change the above condition of 37°C and 100% humidity to NIR (891mW·cm^{-2}). The infrared laser was used to continuously irradiate the central part of the test mold, and the sealed bag was used to wrap the test mold to prevent evaporation of water. The remaining steps were consistent with those described above.

Compressive Strength

After hydration, the upper and lower sections of the cement cylinder samples (CS, CS-1/5/10/20/40$Cu_{2-x}Se$) were gently ground, respectively, and the balance error was 0.01 mm. This was subsequently tested on a mechanical tester with a loading rate of 0.5mm/min. Six samples were measured in each group and averaged.

When exploring the compressive strength of cement paste after NIR irradiation for one hour, it was necessary to irradiate the unformed paste in the mold.[46] On the one hand, the polyethylene tetrafluoride mold has poor thermal conductivity and is prone to heat accumulation leading to temperature rise. On the other hand, the cement paste irradiated by NIR for 1h cannot reach the stripping strength, so it is difficult to test the compressive strength. To this end, we designed and 3D printed aluminum alloy molds that can be directly separated from the middle, have good thermal conductivity, and are easy to release. The cement paste (CS, CS-1/5/10/20/40$Cu_{2-x}Se$) were placed in the aluminum alloy mold, and the upper part of the aluminum alloy mold was carefully removed to ensure that the infrared laser could directly irradiate the cement paste. Then put it in a sealed bag to prevent evaporation of water. After 1h of infrared laser irradiation, the lower part of the aluminum alloy mold was removed to complete the demolding. Six samples were collected from each group and the average value was taken.

Porosity

Porosity directly affects the compressive strength of cement. To determine the porosity of CS-$Cu_{2-x}Se$ cement, samples with a diameter of 6 mm and a height of 12 mm were prepared as described above and dried in a vacuum freeze dryer to maintain the pore shape and size of the hardened paste. After that, the porosity of cement was measured by drainage method. First, the cement was soaked in deionized water, and the weight W1 in water was weighed after it was saturated by vacuum defoaming bucket. After that, the cement sample was removed from the water and dried in a vacuum freeze dryer until the sample weight was constant. The weight W2 in air was weighed, and the appearance volume V of the sample was measured. Six samples were collected from each group and the average value was taken.

The porosity is calculated as follows:

$$P = (W2 - W1)/V \times 100\%$$

Degradation Rate

The controlled degradation of calcium silicate-based cement is clinically essential, as an optimal degradation rate should match the pace of new bone formation. Too rapid degradation may lead to premature loss of mechanical support and reconstruction failure, while overly slow degradation could hinder bone ingrowth and remodeling.[47–49] The degradation properties of four cement formulations (CS, CS-10$Cu_{2-x}Se$, CS-20$Cu_{2-x}Se$, and CS-40$Cu_{2-x}Se$) were investigated according to GB/T16886 standards, with CS serving as the control group to analyze $Cu_{2-x}Se$ concentration-dependent effects on degradation rates. 121.1 g Tris was weighed and dissolved in deionized water, followed by pH adjustment using HCl, volumetric dilution, and sterilization. Disc-shaped cement specimens from all four formulations underwent 72 hour vacuum freeze-drying until constant weight (W3). Tris-HCl solution was added to blue-cap bottles at a 10 mL/cm^2 solution-to-surface-area ratio containing the samples, which were then incubated in a constant-temperature oscillating water bath. Every 5 days, specimens were retrieved, cleaned, dried to record W4, and replenished with fresh Tris-HCl solution. Degradation rate formula:

$$\text{Degradation rate (\%)} = (W3-W4)/W3\times 100\%$$

In vitro Effects on Osteogenesis and Alkaline Phosphatase Activity

Cement specimens (CS and CS-$Cu_{2-x}Se$) cured for 3 days were pulverized and sieved through a 300-mesh screen. Following mass quantification, extracts were prepared by immersing the powder in MEM-α basal medium (200 mg/mL) at 37°C for 24 h. Post-filtration and sterilization, serial dilutions (1/512, 1/256, 1/128, 1/64, 1/32, 1/16, 1/8, 1/4, 1/2) were prepared using MEM-α.

MC3T3-E1 murine pre-osteoblasts (Shanghai Kuisai Biotechnology Co., LTD.) were seeded in 96-well plates at 1×104 cells/well (100 μL suspension in complete medium) and pre-cultured for 24 h (37°C, 5% CO_2). Test groups received cement extracts at specified dilutions, while controls retained MEM-α. At days 1/3/5, cultures were replaced with 90 μL MEM-α + 10 μL CCK-8 reagent. After 2 h incubation, absorbance was measured at 450 nm. There were six samples in each group.

For ALP assessment, cells (2×10^4/well in 48-well plates) were cultured with 1/64-diluted extracts. At day 10, lysates were prepared via centrifugation (discarding supernatant), sonication, and ice-cold extraction. ALP activity was quantified by mixing lysate supernatant with pNPP substrate, measuring 405 nm absorbance after 20 min reaction. Enzymatic units were defined as μmol PNPP hydrolyzed/min/mL at 37°C.

In vitro Immunogenic K7M2-wt Cell Death

In recent years, immunotherapy has become an important breakthrough in the field of cancer treatment, among which ICD has attracted much attention because it can significantly enhance the immunogenicity of tumor cells.[50,51] Studies have shown that ICD induces ATP release, surface calreticulin (CRT) exposure, and high mobility group protein B1 (HMGB-1) nuclear migration of tumor cells, forming a unique "danger signal triad".[52–54] In order to confirm the occurrence of ICD, we detected the ATP release, the membrane translocation of CRT and the nuclear migration of HMGB-1 in tumor cells before and after the intervention of CS-$Cu_{2-x}Se$ cement.

At the wavelength of 340nm, NADPH has a characteristic absorption peak, and the content is positively correlated with ATP, which reflects the intracellular ATP content. Since the thermal conductivity of glass is better than that of plastic, we chose the glass Petri dish with better thermal conductivity, and wrapped the bottom and around the glass Petri dish with aluminum foil. The experiments were divided into four groups: CS, CS+NIR, CS-20$Cu_{2-x}Se$, and CS-20$Cu_{2-x}Se$ +NIR. 10^5 K7M2-wt (Wuhan Purosai Life Science and Technology Co., LTD.) were added to each glass culture dish. For the CS and CS-20$Cu_{2-x}Se$ groups, CS and CS-20$Cu_{2-x}Se$ cement round cakes were placed in the center of the Petri dish and left for 10min, respectively. After that, 500 μL of cold double distilled water was added, the cell suspension was broken in an ice water bath, and a part was removed and extracted for 1min for determination of protein concentration. Another part was bathed in boiling water for 10 min and used for the determination of ATP content. For the CS+NIR group and CS-20$Cu_{2-x}Se$ +NIR group, the procedures were the same as those for the CS and CS-20$Cu_{2-x}Se$ groups, except that 891mW·cm^{-2}, 808nm NIR was used to irradiate the cement cake in the Petri dish for 10min. Finally, the UV-spectrophotometer was preheated for 30min, the wavelength was adjusted to 340 nm, and zero was set using deionized water. The ATP content was calculated according to the instructions of ATP content detection kit. There were three samples in each group.

Regarding the detection of CRT protein and HMGB-1 protein, the procedures used before grouping and placement of cement round cakes were the same as for ATP detection. Sealing was performed using 1% BSA after placement of the cement round cake. Until the detection time point, the medium was discarded and washed three times by adding 1 mL PBS. Then, the cells were fixed with 4% paraformaldehyde for 20 min, blocked with BSA for 30 min, and incubated in the refrigerator overnight with diluted primary antibody (1:100). Diluted fluorescent secondary antibody (1:500) was added and the cells were incubated for 2 h. DAPI dye was added and the cells were incubated in the dark for 5 min. Finally, anti-fluorescence quenching mounting solution was added, and the images were observed under a fluorescence microscope, and the fluorescence intensity was calculated using Image pro plus 7.0 software. There were three samples in each group. Notably, the CRT protein has the ability to escape from the cell and does not require permeabilization before incubation with the primary antibody. HMGB-1 protein does not have the ability to escape from the cells, so before the incubation of

the primary antibody, it needs to be permeabilized with 0.5%Triton X-100 (prepared with PBS) for 20 min at room temperature, and washed with PBS for 3 times to promote HMGB-1 antibody to enter the cytoplasm and bind to it.

Anti-Tumor Effect in vivo

The experiments were divided into four groups: CS, CS+NIR, CS-20$Cu_{2-x}Se$, and CS-20$Cu_{2-x}Se$ +NIR. Nude mice aged 5–6 weeks were selected, and 100 μL of cell dilution (1×10^7 cells /mL) was injected into the armpit of the right forelimb. Each mouse was housed separately and the daily amount of food provided was limited to 5 g. Tumor volume was measured daily, and 0.05mlCS or CS-20$Cu_{2-x}Se$ cement paste was injected when the tumor volume had grown to 50 mm^3. The mice in NIR group were irradiated with NIR ($891mW\cdot cm^{-2}$) for 10min per day, and the mice in non-NIR group were left untreated. The tumor size and body weight of nude mice were measured every 2 days. At 15 days, the nude mice were sacrificed and tumor tissues were obtained. The tumor tissues were fixed in 4% neutral buffered formalin, embedded in paraffin, and stained with hematoxylin and eosin (H&E) after sectioning. The pathological changes were observed under a light microscope. For ethical reasons, mice were sacrificed by cervical dislocation if tumor size exceeded 1000mm^3. There were six samples in each group.

Tumor tissue was also used for immunohistochemistry of CRT protein and HMGB-1 protein. In brief, tumor tissues were fixed with 4% paraformaldehyde for 24h followed by gradient dehydration, paraffin embedding, and sectioning. After decaffinization and hydration, the antigen was repaired by two thermal cycles of sodium citrate buffer. After cooling, the antigen was placed in a wet box and processed sequentially: blocked with 3% hydrogen peroxide for 15min, washed three times with PBS. Goat serum was blocked at 37°C for 30min. CRT (or HMGB-1) primary antibody (1:200) was incubated at 37°C, rewarmed, and washed three times with PBS. Secondary antibodies and streptavidin-HRP were incubated for 30 min each. The DAB color solution developed uniformly for about 8 min, and the microscope was monitored until the brown yellow color was stopped. After he counterstained, the slices were dehydrated in ethanol and transparent in xylene for 25 min, and sealed with neutral gum. The color development time consistency should be controlled during the whole process, and the tissue activity should be maintained by washing with PBS between each step. Finally, the tissue pictures were observed under a microscope and analyzed with Image Pro Plus software.

In vivo Safety Assessment

To assess the short-term toxicity of the materials, non-tumor-bearing mice were divided into CS group and CS-20$Cu_{2-x}Se$ group. The extracts of CS and CS-20$Cu_{2-x}Se$ cement were made by replacing the extracts with MEM-a with sterilized water for injection as described above and filtered to remove bacteria. The CS group was intraperitoneally injected with 100ug CS extract. In the CS-20$Cu_{2-x}Se$ group, 100ug of CS extract was injected. After that, the mice were fed routinely for a week, and the survival status of the two groups of mice was observed and compared. After 7 days, both groups of mice were sacrificed by cervical dislocation, and the heart, liver, spleen, kidney, and lung of the mice were removed for H&E staining analysis to assess in vivo toxicity. There were six samples in each group.

To assess the medium- to long-term toxicity of the materials over a 15-day treatment period, immediately after euthanizing the nude mice from the in vivo experiment, blood was collected via cardiac puncture for serum biochemical analysis. Following the removal of tumor tissue, the heart, liver, spleen, lungs, and kidneys were also harvested for histopathological examination using H&E staining.

For the determination of copper accumulation in the liver via ICP-MS, a portion of liver tissue was rinsed with pre-cooled physiological saline and surface moisture was carefully blotted dry. 100 mg of tissue was accurately weighed and transferred into an acid-resistant digestion tube. High-purity concentrated nitric acid was added, and the sample was thoroughly digested on an electric hot plate until the solution became clear and transparent. After cooling, the digested sample was diluted with ultrapure water and brought to a final volume of 10 mL for subsequent analysis. With the exception of the control group, the six samples in each experimental group were derived from prior in vivo anti-tumor studies.

Statistical Analysis

Statistical analyses were performed using GraphPad Prism software (Version 10), and a power analysis was conducted with SPSSAU. The results are presented as the mean ± standard deviation (SD) and analyzed using one-way analysis of variance (ANOVA) with a post hoc test, whereas the student's *t* - test was used to conduct pairwise comparisons between two groups. The data were considered significantly different when $p < 0.05$.

Results

Characterization of Nano-$Cu_{2-x}Se$

As shown in Figure 1A, the $Cu_{2-x}Se$ nanoparticles, after freeze-drying, appeared as a light, dark brown, flocculent powder with metallic luster under natural light. In Figure 1B, $Cu_{2-x}Se$ nanoparticles dissolved in deionized water presented a clear black-brown solution under natural light after ultrasonic dissolution, and small black particles were not visible to the naked eye. As shown in Figure 1C and D, $Cu_{2-x}Se$ nanoparticles exhibit transverse lattice stripes under TEM, and can also be observed to exhibit a granular round or oval state, with a diameter of about 3nm-5nm measured by the scale bar. As shown in the Figure 1E, the $Cu_{2-x}Se$ nanoparticles exhibit an average hydrodynamic diameter of 190.7 nm in water, due to the absorption of water and subsequent swelling of the PVP coating.

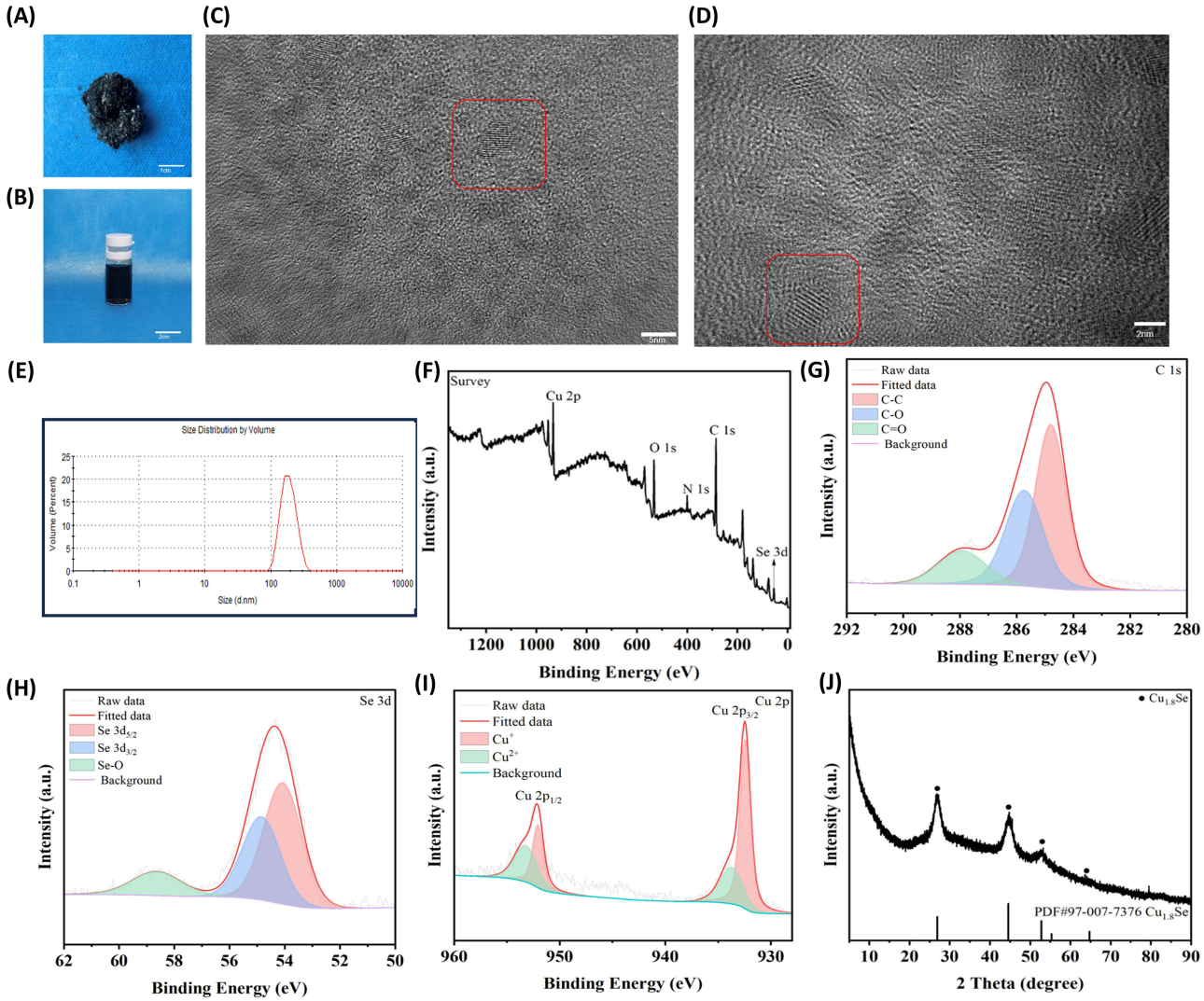

Figure 1 Characterization of nano-$Cu_{2-x}Se$. (**A**) $Cu_{2-x}Se$ after freeze-drying; (**B**) $Cu_{2-x}Se$ aqueous solution; (**C**) TEM (5nm); (**D**) TEM (2nm). In the TEM image, the lattice stripes within the red box represent $Cu_{2-x}Se$ nanoparticles; (**E**) The hydrated particle size of $Cu_{2-x}Se$; (**F**) XPS-wide; (**G**) XPS-Cu; (**H**) XPS-C; (**I**) XPS-Se; (**J**) XRD.

https://doi.org/10.2147/IJN.S548764

In Figure 1F–I: Cu^{+} and Cu^{2+} appear two relatively obvious peaks of Cu element, indicating that Cu does not exist as Cu (I) or Cu (II) alone. Regarding the Se element, there is a clear Se^{2-} peak, which clearly exists as a negative divalent state. The obvious C peak on the C spectrum is due to the fact that we added polyvinylpyrrolidone as a stabilizer during the preparation of copper selenide. As described above, the copper selenide nanoparticles we prepared can be first determined as a mixture of CuSe and Cu_2Se. In addition, the diffraction pattern corresponding to each crystal is also unique, as shown in Figure 1J: By comparing the XRD pattern of $Cu_{2-x}Se$ nanoparticles with the JCPDS card and combining with the XPS results, the molecular formula of copper selenide nanoparticles can be confirmed to be $Cu_{2-x}Se$.

Characterization of CS-$Cu_{2-x}Se$

As shown in Figure 2A–F, six groups of cylindrical cement specimens (6×12 mm) and disc-shaped bone cement specimens (10×2 mm) were prepared, designated as CS, CS-1$Cu_{2-x}Se$, CS-5$Cu_{2-x}Se$, CS-10$Cu_{2-x}Se$, CS-20$Cu_{2-x}Se$, and CS-40$Cu_{2-x}Se$. No significant differences in color or appearance were observed among the various compositions.

The phase analysis of CS powder through XRD patterns (Figure 2G) compared with JCPDS cards revealed the presence of abundant tricalcium silicate crystals. As illustrated in Figure 2H, the XRD patterns demonstrated both unreacted tricalcium silicate crystals and hydration-generated $Ca(OH)_2$. Comparatively, the CS-1$Cu_{2-x}Se$ and CS-5$Cu_{2-x}Se$ groups showed no significant differences in $Ca(OH)_2$ diffraction peaks relative to the control CS group. However, CS-10$Cu_{2-x}Se$, CS-20$Cu_{2-x}Se$, and CS-40$Cu_{2-x}Se$ exhibited enhanced $Ca(OH)_2$ diffraction peaks compared to CS cement, with particularly noticeable intensity increases at the 18° peak. This suggests that the addition of 0.1–0.4 wt% $Cu_{2-x}Se$ nanoparticles might promote $Ca(OH)_2$ crystallization. Notably, the $Ca(OH)_2$ diffraction peaks of CS-10$Cu_{2-x}Se$ and CS-20$Cu_{2-x}Se$ surpassed those of CS-40$Cu_{2-x}Se$, potentially indicating that excessive $Cu_{2-x}Se$ nanoparticle concentration (0.4 wt%) inhibits $Ca(OH)_2$ crystallization.

SEM observations at 1000× magnification (Figure 2I) revealed that all samples primarily consisted of uniformly sized blocky particles (5–10 μm) with distinct porous structures, likely formed by agglomeration of unhydrated C_3S and hydration products ($Ca(OH)_2$ and C-S-H. Needle-like crystals surrounding the particles exhibited typical early-stage C-S-H hydration characteristics. The absence of direct $Cu_{2-x}Se$ observation under SEM might be attributed to its small

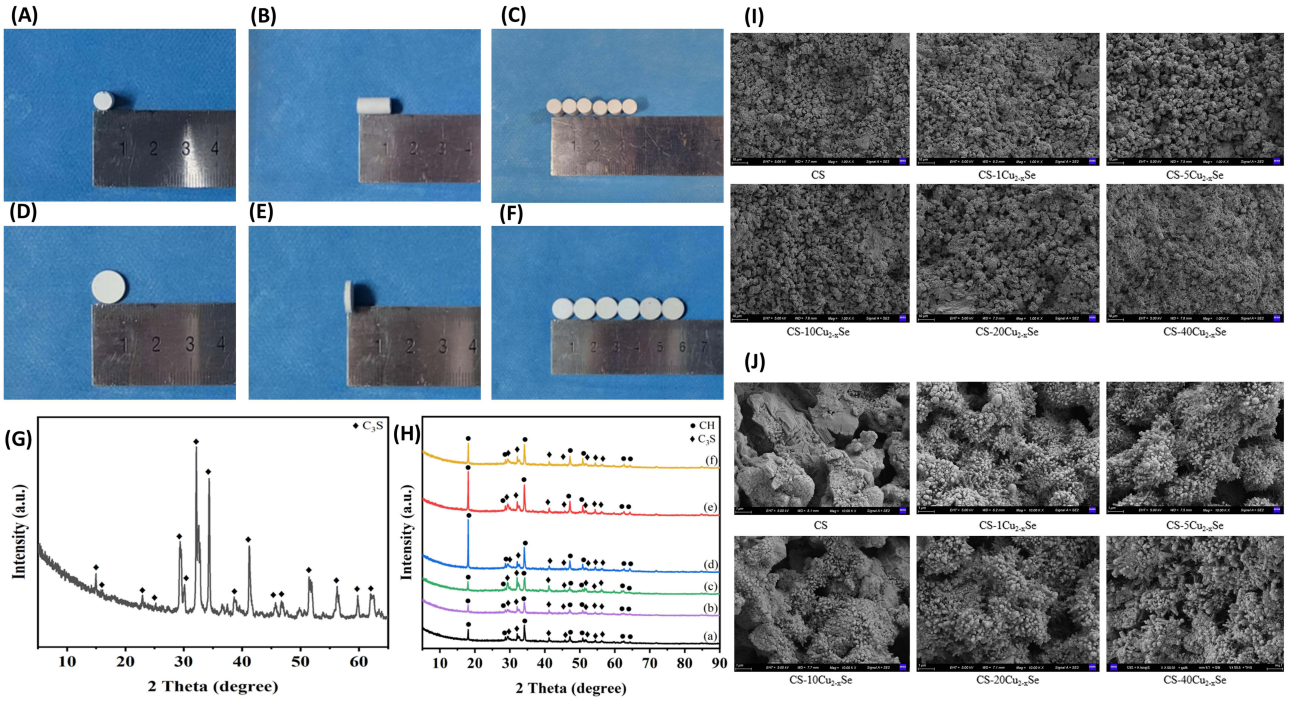

Figure 2 Characterization of CS-$Cu_{2-x}Se$. (**A–F**) General view of CS-$Cu_{2-x}Se$. (**G**) CRD. (**H**) The XRD results of CS-$Cu_{2-x}Se$ showed that a-f was CS, CS-1$Cu_{2-x}Se$, CS-5$Cu_{2-x}Se$, CS-10$Cu_{2-x}Se$, CS-20$Cu_{2-x}Se$ and CS-40$Cu_{2-x}Se$, respectively. (**I**) Cross section morphology of cement under SEM (1000 times). (**J**) Cross section morphology of cement under SEM (10000 times).

particle size and low content. However, 10000× magnification (Figure 2J) revealed plate-like structures enveloped by acicular morphologies in hydrated cement. Considering the lamellar aggregation state of $Cu_{2-x}Se$, these negatively charged plate-like structures could enhance hydration reactions. It can be concluded that the lamellar $Cu_{2-x}Se$ aggregates might become encapsulated by cement hydration products, forming these distinctive plate-like hydration products.

Photothermal Properties

As shown in Figure 3A–N), the temperatures of all cement paste and hydrated cement increased under NIR (891 $mW \cdot cm^{-2}$) irradiation and stabilized after 200s until the end of irradiation. The temperature variation exhibited a progressive enhancement with increasing $Cu_{2-x}Se$ content, demonstrating that the incorporation of $Cu_{2-x}Se$ imparted photothermal properties to CS, which were already present in the paste state. Notably, the elevated temperatures achieved by CS-20$Cu_{2-x}Se$ and CS-40$Cu_{2-x}Se$ pastes reached levels sufficient for tumor ablation. The photothermal functionality could be activated prior to complete solidification of the paste, suggesting potential clinical applicability for early-stage irradiation treatment immediately after paste injection.

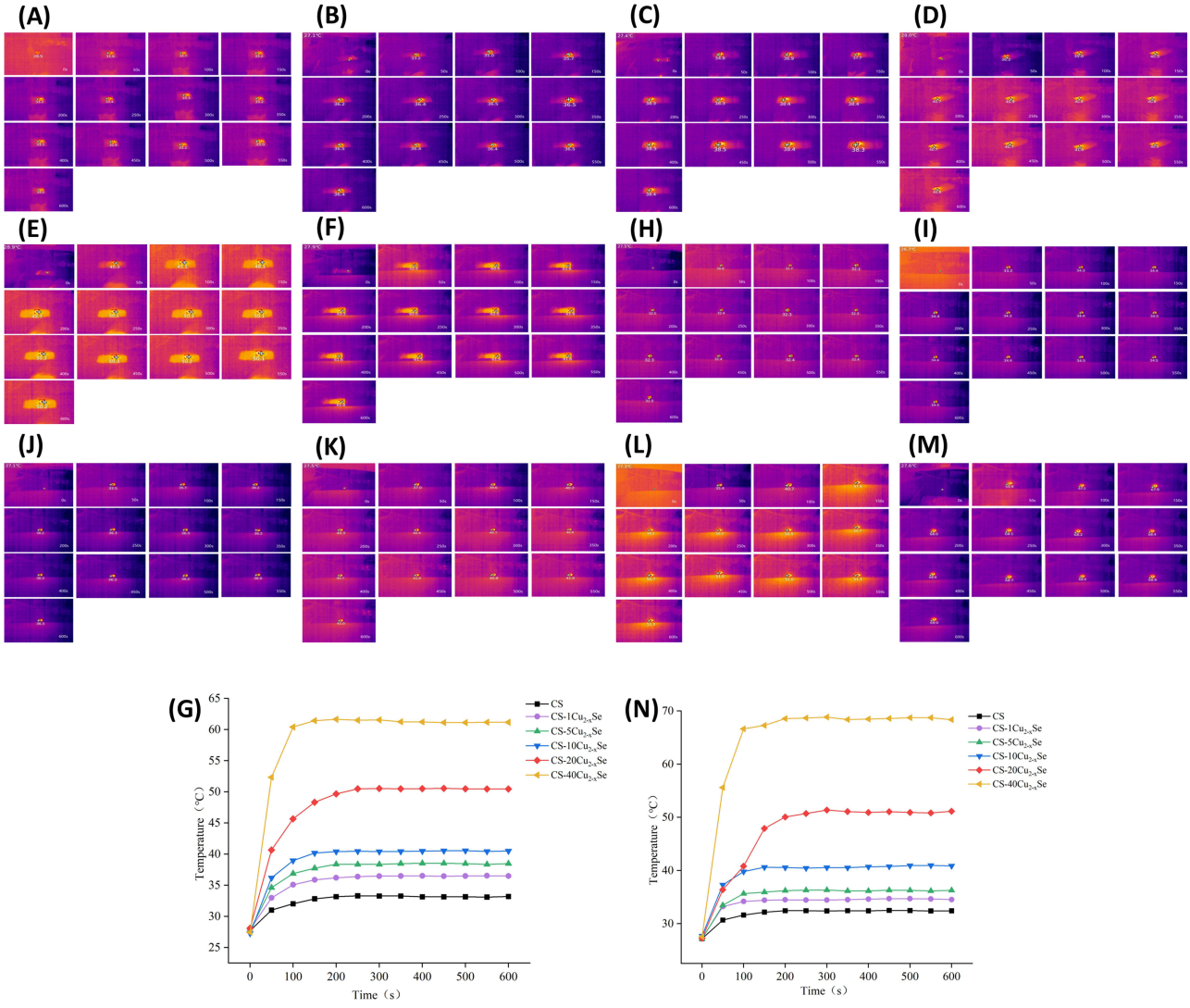

Figure 3 Photothermal images of CS-$Cu_{2-x}Se$ within 0~600s at a NIR power of 891mW $\cdot cm^{-2}$. (**A**–**F**) Cement paste, followed by CS, CS-1$Cu_{2-x}Se$, CS-5$Cu_{2-x}Se$, CS-10Cu_{2-x}Se, CS-20$Cu_{2-x}Se$, and CS-40$Cu_{2-x}Se$. (**G**) Temperature changes of different components of bone cement paste under NIR. (**H**–**M**) After hydration, followed by CS, CS-1$Cu_{2-x}Se$, CS-5$Cu_{2-x}Se$, CS-10$Cu_{2-x}Se$, CS-20$Cu_{2-x}Se$. (N) Temperature changes of different components of hydrated cement under NIR. In (a~m), "+" represents the highest temperature point in the figure, and the numbers beside it indicate the temperature values.

https://doi.org/10.2147/IJN.S548764

Although the CS cement paste exhibited an average temperature increase of 4.5°C and the solidified CS cement showed a 4.9°C rise-demonstrating minimal inherent photothermal conversion capacity-these thermal variations were negligible compared to the other five groups containing $Cu_{2-x}Se$. Furthermore, the resultant temperatures remained insufficient for tumor ablation. Consequently, in subsequent experimental protocols, CS was considered devoid of practical photothermal conversion capability.

Accordingly, the photothermal conversion efficiency (η) was calculated based on the measured parameters. The maximum temperature (T_{max}) of the solution under irradiation was 47 °C, against an ambient temperature (T_{surr}) of 25 °C. During the cooling phase, the temperature recorded at t = 40s after the laser was turned off was 43 °C. Based on these values, the photothermal conversion efficiency (η) was determined to be 50.58%. This value is higher than that of copper selenide prepared by other methods described in Wang's article (the maximum being 30.8%).

Final Setting Time

As shown in Figure 4A, under 37°C and saturated water vapor conditions, the incorporation of $Cu_{2-x}Se$ reduced the setting time of CS-$Cu_{2-x}Se$ paste. Pure CS cement exhibited an average setting time of 155 min, while the final setting times for CS-1$Cu_{2-x}Se$, CS-5$Cu_{2-x}Se$, CS-10$Cu_{2-x}Se$, CS-20$Cu_{2-x}Se$, and CS-40$Cu_{2-x}Se$ averaged 152, 150, 135, and 112 min, respectively. The progressive decrease in final setting time with increasing $Cu_{2-x}Se$ content indicates accelerated CS hydration through $Cu_{2-x}Se$ incorporation, consistent with the XRD findings in Section "Characterization of CS-Cu_{2-x}Se" regarding $Cu_{2-x}Se$ enhanced hydration. It is important to note that while the cement has set at this stage, it is far from achieving sufficient demolding strength. This accurately mirrors the clinical scenario where the newly formed bone cement, though solidified, cannot yet bear physiological loads.

Figure 4B demonstrates that NIR-induced temperature elevation accelerated both the setting process and hydration degree of CS-$Cu_{2-x}Se$. When irradiated with 808 nm NIR light, the photothermal properties of the composite cement significantly expedited the setting process. CS-40$Cu_{2-x}Se$ exhibited a markedly reduced average setting time of 65 min under irradiation compared to its non-irradiated counterpart (112 min). Similarly, CS-5$Cu_{2-x}Se$, CS-10$Cu_{2-x}Se$, and CS-20$Cu_{2-x}Se$ demonstrated substantial reductions in solidification times, averaging 144, 123, and 92 min, respectively.

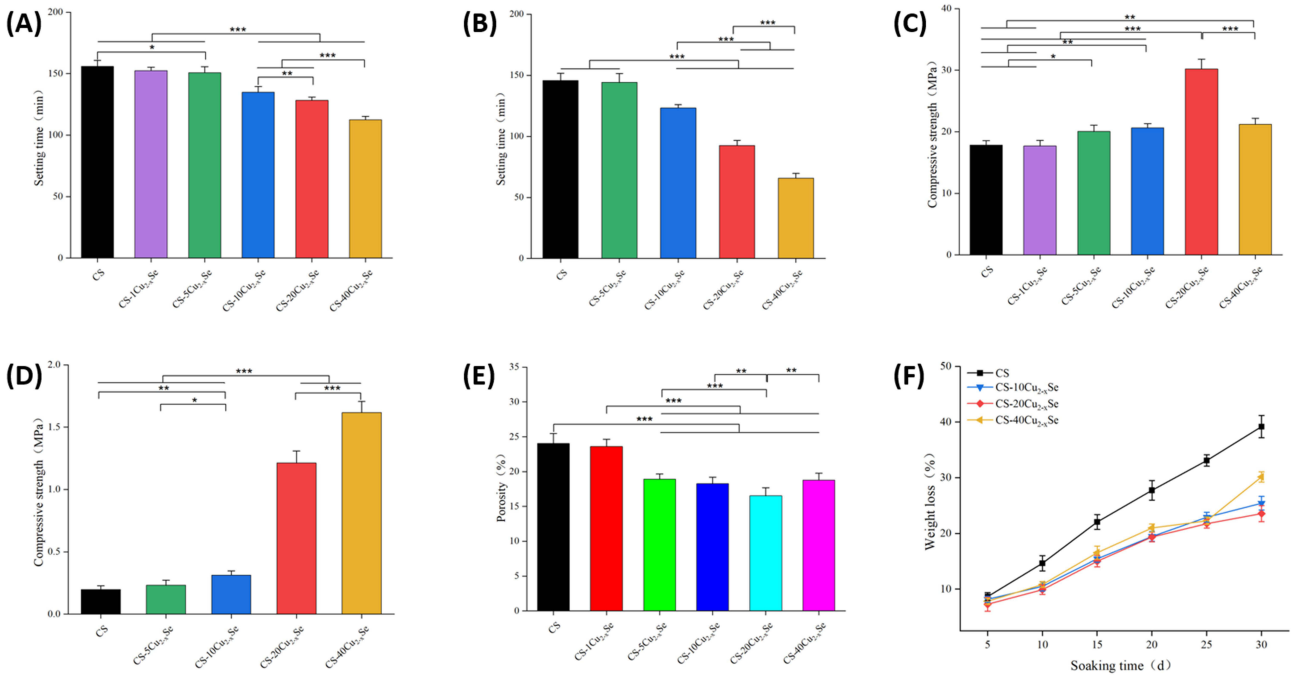

Figure 4 General properties of CS-$Cu_{2-x}Se$ (**A**) Final setting time at 37 °C, 100% humidity. (**B**) Final setting time under NIR power of 891mW·cm^{-2} irradiation at 37 °C, 100% humidity. (**C**) Compressive strength of cement hydrated for 24 h at 37 ° C and 100% humidity. (**D**) Compressive strength of paste irradiated with NIR at 891mW·cm^{-2} for 1h. (**E**) Porosity of each component of cement. (**F**) Degradation rate of each component of cement. (*p<0.05, **p<0.01, ***p<0.001).

Setting time is critical for clinical bone cement applications, where shorter durations minimize pre-solidification extravasation risks and enable early mechanical strength post-implantation.[55,56] The photothermal characteristics of CS-$Cu_{2-x}Se$ cement thus provide distinct advantages in adjustable setting time. Considering potential thermal damage to normal tissues, temperatures should be maintained below 55°C during this process.

Compressive Strength

As shown in Figure 4C, the compressive strength of CS-$Cu_{2-x}Se$ initially increased with $Cu_{2-x}Se$ content, rising from an average of 17.85 MPa (CS) to 20.06 MPa (CS-5$Cu_{2-x}Se$), 20.64 MPa (CS-10$Cu_{2-x}Se$), and 30.21 MPa (CS-20$Cu_{2-x}Se$), but declined to 21.21 MPa when $Cu_{2-x}Se$ content reached 0.4 wt% (CS-40$Cu_{2-x}Se$). It has been reported that CS particles release Ca^{2+} and SiO_3^{2-} ions during hydration.[57] Nanoscale calcium silicate hydrate (C-S-H) gel preferentially nucleates and deposits around CS particles.[56,58] In CS-$Cu_{2-x}Se$ composites, the presence of $Cu_{2-x}Se$ provides additional nucleation sites due to its negatively charged surfaces. This accelerates Ca^{2+} deposition rates and C-S-H nucleation kinetics, thereby enhancing both the setting process and compressive strength of CS-$Cu_{2-x}Se$ cement.

Regarding the effects of NIR on final setting time, we conclude that 808 nm NIR irradiation significantly accelerates the setting process of CS-$Cu_{2-x}Se$ paste. Figure 4D reveals notable compressive strength enhancement in NIR-irradiated CS-$Cu_{2-x}Se$ specimens. The irradiated CS-40$Cu_{2-x}Se$ achieved an average compressive strength of 1.61 MPa, surpassing values for CS (0.19 MPa), CS-5$Cu_{2-x}Se$ (0.23 MPa), CS-10$Cu_{2-x}Se$ (0.31 MPa), and CS-20$Cu_{2-x}Se$ (1.21 MPa). This improvement likely stems from NIR-induced thermal effects that expedite both the setting process and hydration degree of CS-$Cu_{2-x}Se$ paste.

Porosity

As shown in Figure 4E, the porosity of the cement exhibited an inverse trend compared to the compressive strength changes depicted in Figure 4C. With increasing $Cu_{2-x}Se$ content, the porosity of CS-$Cu_{2-x}Se$ progressively decreased from an average of 24.0% (CS) to 23.6% (CS-1Cu2-xSe), 18.9% (CS-5Cu2-xSe), 18.2% (CS-10Cu2-xSe), and 16.5% (CS-20$Cu_{2-x}Se$), but rebounded to 18.4% when $Cu_{2-x}Se$ content reached 0.4 wt% (CS-40$Cu_{2-x}Se$). As discussed in Section 3.6, the $Cu_{2-x}Se$-induced enhancement of C-S-H nucleation occurred not only on CS particle surfaces but also within the pores of the cement matrix, leading to reduced porosity in CS-$Cu_{2-x}Se$ composites. However, when $Cu_{2-x}Se$ content exceeded 0.4 wt%, the C-S-H structure likely became more disordered, paradoxically resulting in increased porosity for CS-40$Cu_{2-x}Se$ cement.

Degradation Rate

As shown in Figure 4F, no significant differences in degradation rates were observed among CS, CS-10$Cu_{2-x}Se$, CS-20$Cu_{2-x}Se$, and CS-40$Cu_{2-x}Se$ at 5 d. During the 10–30 d period, however, CS-10$Cu_{2-x}Se$, CS-20$Cu_{2-x}Se$, and CS-40$Cu_{2-x}Se$ exhibited markedly slower degradation compared to CS. At 30 d, CS-20$Cu_{2-x}Se$ demonstrated the lowest degradation rate (23.57%), outperforming CS-10$Cu_{2-x}Se$ (25.43%) and CS-40$Cu_{2-x}Se$ (30.16%). This observation aligns with the aforementioned acceleration of hydration processes and reduced porosity induced by $Cu_{2-x}Se$ incorporation, suggesting potential suitability for osteosarcoma treatment cycles through sustained functionality, and demonstrating significant clinical application prospects.

In vitro Effects on MC3T3-E1 Cell Proliferation and Alkaline Phosphatase Activity

As shown in Figure 5A, MC3T3-E1 cells cultured in 1/64 to 1/512 dilutions of CS and CS-$Cu_{2-x}Se$ extracts exhibited survival rates consistently exceeding those of the control group (MEM-α). Furthermore, no significant differences in cellular proliferation behavior were observed between CS and CS-$Cu_{2-x}Se$ extracts, indicating that the incorporation of $Cu_{2-x}Se$ nanoparticles did not adversely affect the in vitro cytocompatibility of CS.

Regarding the influence of cement extracts on ALP activity, Figure 5B demonstrates that 1/64 dilutions of both CS and CS-20$Cu_{2-x}Se$ stimulated ALP activity in MC3T3-E1 cells, with CS-20$Cu_{2-x}Se$ exhibiting superior stimulation compared to CS. These results confirm that CS-20$Cu_{2-x}Se$ retains the bioactivity of CS while enhancing MC3T3-E1 cell proliferation and ALP activity expression. The stronger ALP stimulation observed in CS-20$Cu_{2-x}Se$ may correlate

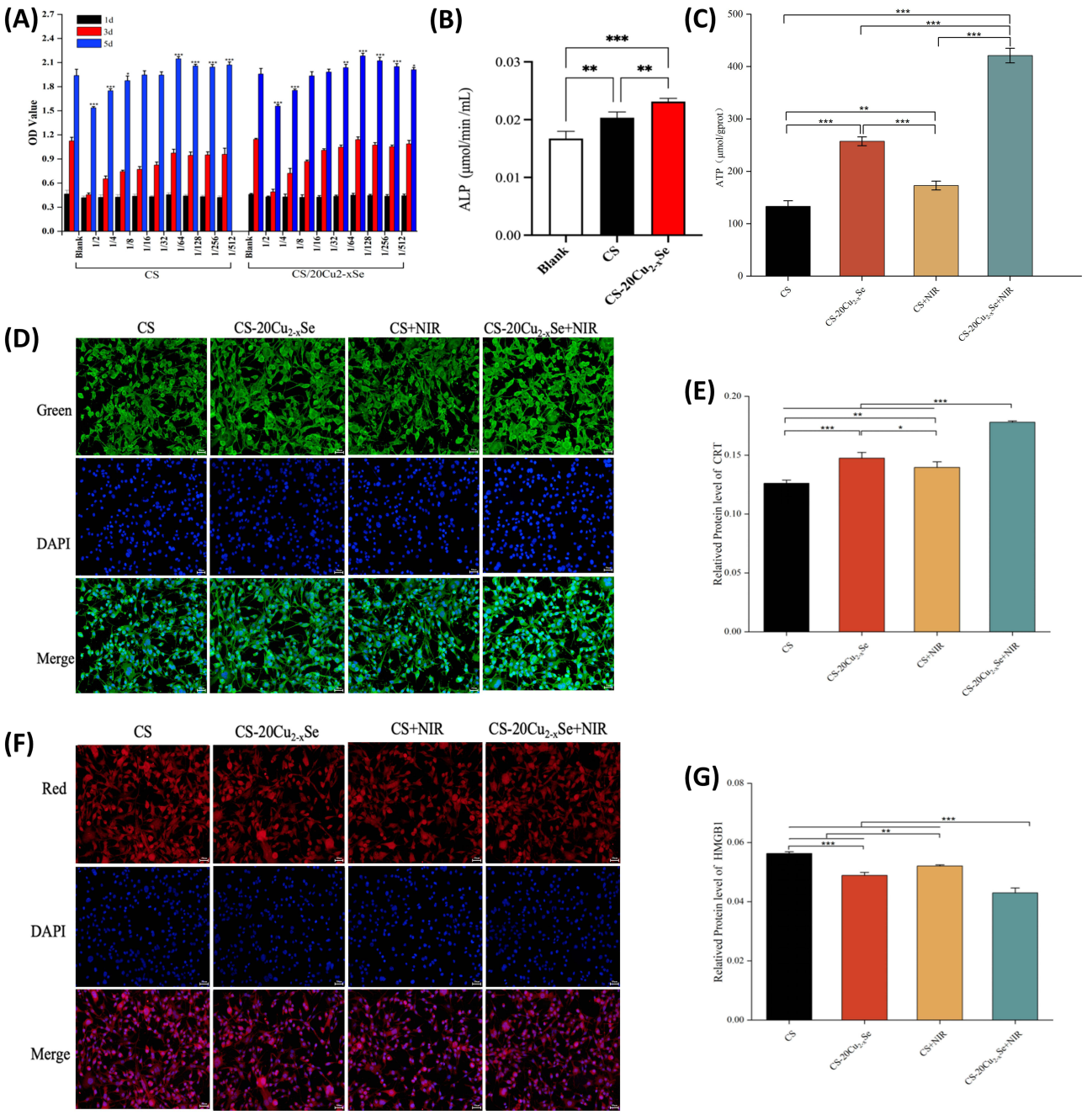

Figure 5 In vitro effect of bone cement on MC3T3-E1 cells and K7M2-wt cells. (**A**) MC3T3-E1 cell proliferation assay. (**B**) ALP activity assay. (**C**) CS-$Cu_{2-x}Se$ combined with NIR caused ATP release from K7M2-wt cells. (**D**) CRT protein visualized by fluorescence microscopy. (**E**) CRT protein content. (**F**) HMGB-1 protein under fluorescence microscopy. (**G**) HMGB-1 protein content. (*p<0.05, **p<0.01, ***p<0.001).

with the osteogenic activity-enhancing effects of specific concentrations of Cu^{2+} and Cu^{+} ions. Collectively, these findings highlight the favorable biocompatibility of CS-$Cu_{2-x}Se$, strongly supporting CS-20$Cu_{2-x}Se$ as a promising bioactive material for bone defect repair applications.

In vitro Induction of Immunogenic K7M2-wt Cell Death

As shown in Figure 5C, using the CS group as the control, the CS+NIR group demonstrated stronger ATP release than CS alone but remained substantially lower than CS-20$Cu_{2-x}Se$+NIR. This indicates that while NIR mediation played a partial role (potentially linked to localized temperature elevation in CS under irradiation), it was not the primary driver

for promoting ICD and subsequent ATP secretion. The CS-20Cu_{2-x}Se group exhibited greater ATP release compared to both CS and CS+NIR groups, suggesting that Cu_{2-x}Se nanoparticles induce ICD-mediated ATP secretion, likely through their peroxidase-mimetic activity that elevates intracellular ROS levels in tumor cells. The CS-20Cu_{2-x}Se+NIR group displayed the highest ATP levels—over threefold higher than CS alone and approximately double those of CS-20Cu_{2-x}Se and CS+NIR groups—attributable to synergistic effects of thermal enhancement and Cu_{2-x}Se's enzyme-like activity. Notably, literature reports confirm that the enzymatic activity of CS-20Cu_{2-x}Se intensifies with temperature elevation, achieving coordinated antitumor efficacy.[59] These findings collectively demonstrate that Cu_{2-x}Se incorporation and NIR irradiation synergistically stimulate extracellular ATP release in vitro, surpassing the effects of CS alone.

In Figure 5D, the CS-20Cu_{2-x}Se+NIR group exhibited stronger fluorescence intensity than other groups, characterized by blue nuclei and intense green fluorescent protein signals. Minimal differences were observed among CS, CS+NIR, and CS-20Cu_{2-x}Se groups. As shown in Figure 5E, Quantitative analysis using Image-Pro Plus 7.0 revealed relative fluorescence intensities of 0.1780 (CS-20Cu_{2-x}Se+NIR), 0.1475 (CS-20Cu_{2-x}Se), 0.1396 (CS+NIR), and 0.1261 (CS), aligning with ATP release trends. Compared to the CS control, both Cu_{2-x}Se incorporation and NIR irradiation elevated CRT protein levels, with their combination producing the most pronounced enhancement. As CRT serves as a critical pro-apoptotic protein, these results confirm that CS-20Cu_{2-x}Se+NIR induces significant ICD in K7M2-wt cells.

Figure 5F shows HMGB-1 protein fluorescence patterns analogous to CRT observations, yet contrary to the trends observed in ATP release and CRT protein detection. Image-Pro Plus 7.0 analysis yielded relative fluorescence intensities of 0.0430 (CS-20Cu_{2-x}Se+NIR), 0.0489 (CS-20Cu_{2-x}Se), 0.0521 (CS+NIR), and 0.0563 (CS) in Figure 5G. Relative to the CS control, both Cu_{2-x}Se incorporation and NIR irradiation reduced HMGB-1 levels, with their combination exerting the strongest inhibitory effect. Given HMGB-1's role as an anti-apoptotic protein, this suppression further corroborates that CS-20Cu_{2-x}Se under 808 nm NIR irradiation effectively induces ICD in K7M2-wt cells.

In vivo Photothermal Effect

As shown in Figure 6A, three untreated nude mice received 600 s NIR (891 $mW \cdot cm^{-2}$) irradiation on upper, middle, and lower axillary skin regions, with a maximum recorded temperature of 37.2°C. This confirms the safety of the selected NIR power for in vivo applications, ensuring no thermal injury to murine skin during experimental interventions.

Figure 6B demonstrates that NIR irradiation elevated tumor site temperatures in the CS group from an average baseline of 36.3°C to 39.4°C, yielding a mean temperature increase of 3.1°C. In contrast, the CS-20Cu_{2-x}Se+NIR group (Figure 6C) exhibited a dramatic temperature rise from 35.9°C to 50.8°C at tumor sites, achieving a 14.9°C increment nearly fivefold greater than the CS group. As illustrated in Figure 6D, tumor site temperatures in the CS-20Cu_{2-x}Se group rapidly reached approximately 50°C within 200 s of NIR exposure, stabilizing at this tumor-ablation-effective temperature throughout irradiation. These results confirm the exceptional in vivo photothermal performance of CS-Cu_{2-x}Se, demonstrating its potential for clinical bone sarcoma ablation applications.

In vivo Antitumor Effect

As shown in Figure 6E and F, the CS-20Cu_{2-x}Se+NIR group demonstrated a tumor volume reduction trend, decreasing to 46 mm^3 (<50 mm^3) by day 14. Conversely, tumor volumes increased significantly in the CS, CS+NIR, and CS-20Cu_{2-x}Se groups. The CS group exhibited tumor growth to 820 mm^3 by day 14, reaching 1023 mm^3 prior to cervical dislocation at day 15. Tumors in the CS+NIR and CS-20Cu_{2-x}Se groups measured 179 mm^3 and 303 mm^3, respectively, at day 14. Notably, the CS+NIR group showed superior therapeutic efficacy compared to CS-20Cu_{2-x}Se in vivo, contrasting with in vitro findings. This observed discrepancy can likely be attributed to the physical and chemical barriers present in the solid tumor microenvironment, which impede drug penetration and distribution, thereby diminishing the therapeutic outcome.[60,61] Furthermore, NIR itself exerts a certain inhibitory effect on tumor growth in vivo,[62] which may account for the differences observed compared to in vitro experiments.

Figure 6H reveals distinct histopathological differences: the CS-20Cu_{2-x}Se+NIR group displayed disorganized tumor architecture with extensive necrosis, cellular debris reduction, and hemorrhage. In contrast, the CS group maintained intact tumor structures with densely packed and uniformly arranged cells. Although CS+NIR and CS-20Cu_{2-x}Se groups

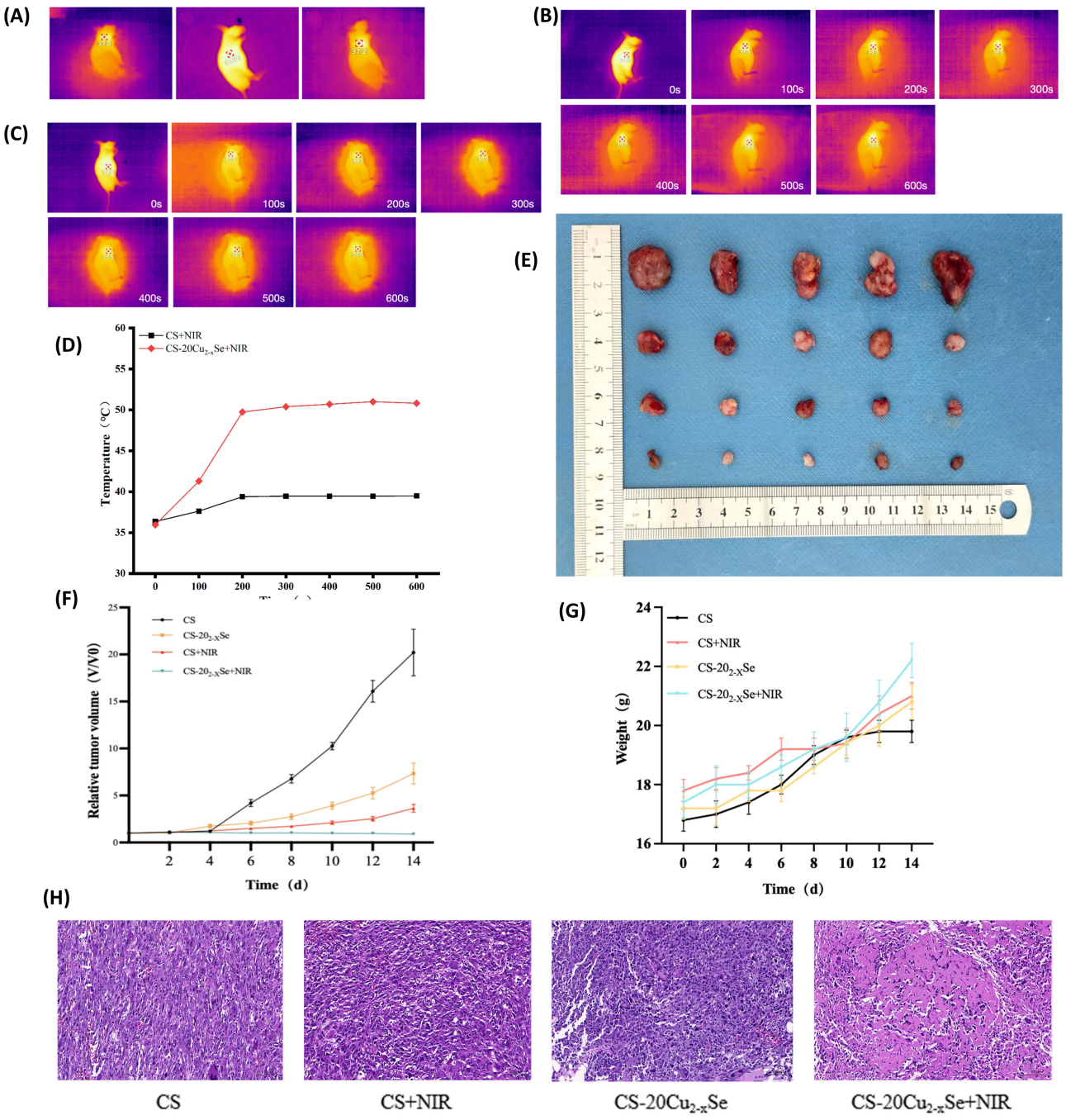

Figure 6 In vivo anti-tumor efficacy and safety of bone cement. (**A**) Safety assessment of NIR bioapplication at 891mW·cm^{-2}. (**B**) Temperature monitoring in nude mice injected with CS of NIR bioapplication at 891mW·cm^{-2}. (**C**) Temperature monitoring in nude mice injected with CS-1Cu$_{2-x}$Se of NIR bioapplication at 891mW·cm^{-2}. (**D**) Temperature changes in nude mice injected with CS and CS-20Cu$_{2-x}$Se after NIR irradiation with 891mW·cm^{-2}. (**E**) Tumor size changes over 14 days. (**F**) The relative tumor volume changes over 14 days. (**G**) Weight changes in mice over 14 days. (**H**) Macroscopic view of the tumor tissue at day 15.

exhibited slower tumor growth than CS controls, neither showed significant cellular damage under microscopic examination. These findings confirm that CS-20Cu$_{2-x}$Se+NIR induces irreversible photothermal tumor destruction.

Furthermore, Figure 6G illustrates body weight increases throughout the treatment period for CS+NIR, CS-20Cu$_{2-x}$Se, and CS-20Cu$_{2-x}$Se+NIR groups. The CS group showed weight loss by day 14, potentially associated with tumor progression. While both CS+NIR and CS-20Cu$_{2-x}$Se partially inhibited tumor growth, only CS-20Cu$_{2-x}$Se+NIR achieved tumor ablation with sustained volume reduction.

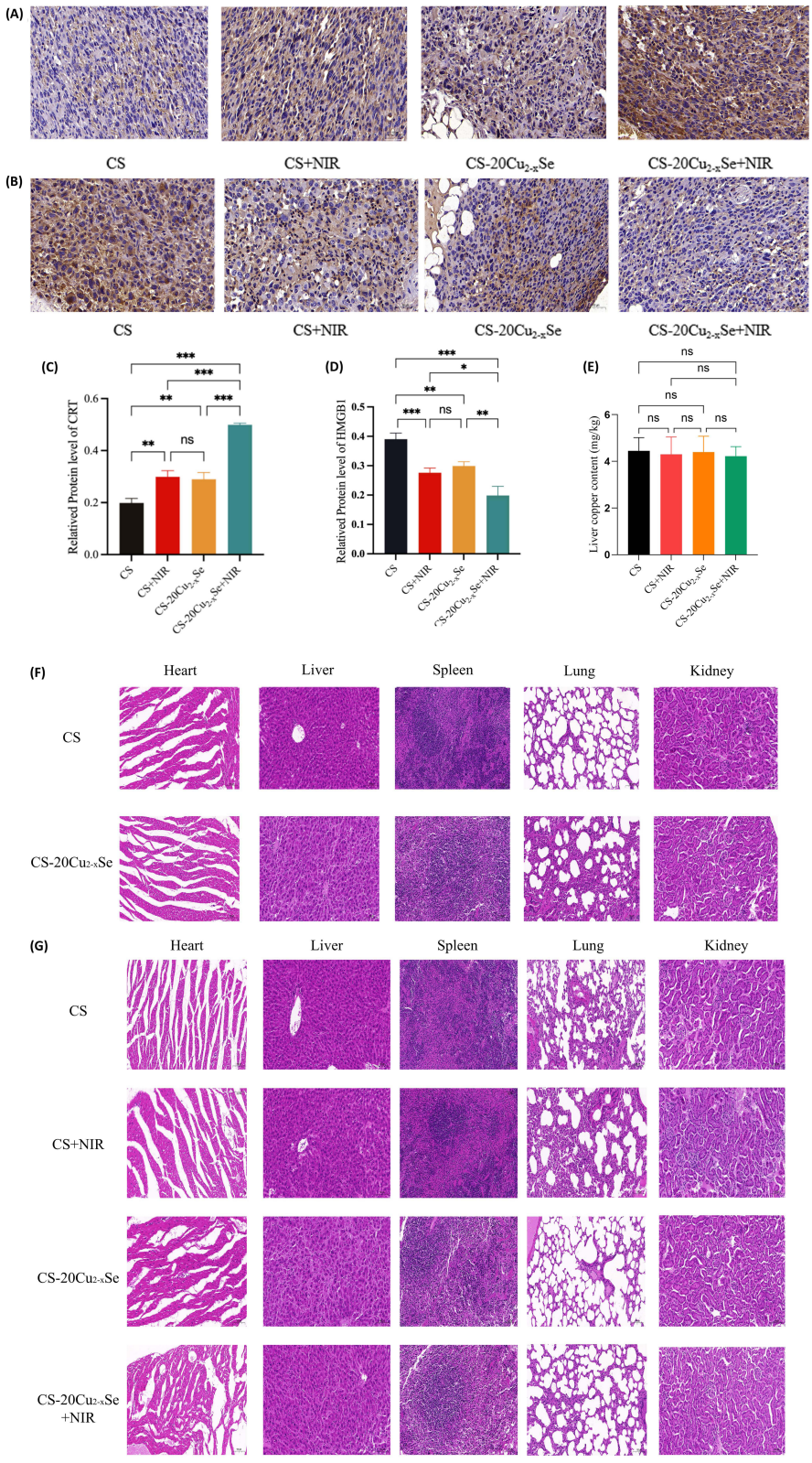

Figure 7 Bone cement-induced ICD and safety assessment in vivo. (**A**) CRT immunohistochemistry in tumor tissue. (**B**) Immunohistochemistry of HMGB-1 in tumor tissue. (**C**) Immunohistochemical intensity analysis of CRT protein. (**D**) Immunohistochemical intensity analysis of HMGB-1 protein. (**E**) The copper content in the liver over a period of 15 days. (**F**) Tissue sections from the viscera of nude mice at day 7. (**G**) Tissue sections from the viscera of nude mice at day 15. (*p<0.05, **p<0.01, ***p<0.001. ns, not significant).

https://doi.org/10.2147/IJN.S548764

In vivo Detection of ICD Markers

As shown in Figure 7A, fluorescence microscopy revealed the deepest brown coloration in the CS-20Cu_{2-x}Se+NIR group and the lightest in the CS group, with CS-20Cu_{2-x}Se and CS+NIR groups exhibiting intermediate staining intensities that were visually indistinguishable. Quantitative analysis using Image-Pro Plus 7.0 yielded average optical density values (Figure 7C), showing relative fluorescence intensities of 0.4988 (CS-20Cu_{2-x}Se+NIR), 0.2896 (CS-20Cu2-xSe), 0.2993 (CS+NIR), and 0.1988 (CS). Compared to the CS control, both Cu_{2-x}Se incorporation and NIR irradiation independently enhanced calreticulin (CRT) protein levels without statistical significance between these individual interventions. However, their combination in CS-20Cu_{2-x}Se+NIR synergistically amplified CRT expression to the greatest extent.

Figure 7B displays an inverse fluorescence pattern for HMGB-1 protein, with the strongest signal in the CS group and the weakest in CS-20Cu_{2-x}Se+NIR, while CS-20Cu_{2-x}Se and CS+NIR groups showed intermediate intensities. Image-Pro Plus 7.0 analysis (referenced in Figure7D) quantified relative fluorescence intensities as 0.1985 (CS-20Cu_{2-x}Se+NIR), 0.2987 (CS-20Cu_{2-x}Se), 0.2760 (CS+NIR), and 0.3896 (CS). Relative to the CS control, Cu_{2-x}Se incorporation and NIR irradiation individually reduced HMGB-1 levels without statistically significant differences between them. The combined CS-20Cu_{2-x}Se+NIR treatment demonstrated synergistic suppression of HMGB-1, most effectively promoting ICD in K7M2-wt cells.

In vivo Safety

As shown in Figure 7E, the liver copper content in mice treated with CS-Cu_{2-x}Se and CS-Cu_{2-x}Se+NIR was comparable to that in the CS and CS+NIR control groups, with no statistically significant differences. Furthermore, examination of H&E-stained sections (Figure 7F–G) from major organs revealed no significant pathological abnormalities under the microscope. In addition, the liver and kidney function indicators presented in Table 1 were comparable to those of the control group, with no statistically significant differences observed. Taken together, the data from one full treatment cycle suggest that the administration of CS-Cu_{2-x}Se bone cement did not reveal significant toxicity or copper accumulation attributable to the material within the observed timeframe.

Conclusion

This study successfully developed photothermally active Cu_{2-x}Se nanoparticles and integrated them into a calcium silicate matrix to fabricate CS-Cu_{2-x}Se composite bone cement with combined bone-regenerative and antitumor functions. In vitro assays confirmed that CS-20Cu_{2-x}Se maintained the bioactivity of pure CS, as evidenced by enhanced proliferation of MC3T3-E1 pre-osteoblasts and increased ALP expression. While CS+NIR and CS-20Cu_{2-x}Se alone induced moderate ICD in K7M2-wt cells, the CS-20Cu_{2-x}Se+NIR group exhibited markedly stronger ICD effects, as validated by elevated ATP release and enhanced CRT and HMGB1 exposure. These results underscore a synergistic antitumor interaction between Cu_{2-x}Se and near-infrared irradiation. In a murine model, CS-20Cu_{2-x}Se+NIR treatment led to significant tumor ablation, in contrast to progressive tumor growth observed in control groups. Histopathological

Table 1 Main Indicators of Liver and Kidney Functions in Nude Mice

Groups / Indexes	Control	CS	CS+NIR	CS-Cu_{2-x}Se	CS-Cu_{2-x}Se +NIR
ALT	44.4 ± 7.3	51.4 ± 9.1	46.7 ± 5.1	43.1 ± 10.6	48.7 ± 8.4 ^{ns}
AST	161.1 ± 16.3	164.2 ± 13.3	160.4 ± 18.4	155.9 ± 18.9	162.7 ± 15.3 ^{ns}
ALP	141.9 ± 28.9	165.5 ± 27.2	173.5 ± 28.8	175.2 ± 21.9	176.1 ± 30.4 ^{ns}
TBIL	< 1.7	< 1.7	< 1.7	< 1.7	< 1.7 ^{ns}
ALB	28.1 ± 2.8	30.5 ± 1.9	31.7 ± 2.4	28.4 ± 2.2	25.1 ± 3.1 ^{ns}
CREA	38.3 ± 7.5	31.5 ± 7.9	35.1 ± 4.9	37.5 ± 8.1	33.6 ± 5.8 ^{ns}
BUN	8.1 ± 1.4	6.9 ± 2.1	8.1 ± 1.9	7.8 ± 2.3	6.6 ± 1.8 ^{ns}

Abbreviations: ALT, Alamine aminotransferase; AST, Aspartic transaminase; ALP, Alkaline phosphatase; TBIL, Total bilirubine tbil; ALB, Albumin; CREA, Serum creatinine; BUN, Blood urea nitrogen; ns, Not significant.

evaluation further confirmed extensive tumor necrosis and decreased HMGB1 expression, supporting the efficacy of the combinational therapy.

The biosafety of CS-20$Cu_{2-x}Se$ was systematically evaluated. Assessments of copper accumulation in the liver, blood biochemistry for liver and kidney function, and H&E staining of major organs revealed no significant signs of systemic toxicity. Nevertheless, this study has several limitations. Certain material properties, such as standard consistency and tensile strength, were not fully characterized, and enzymatic activities including peroxidase-like behavior and ROS generation were not quantitatively examined. Moreover, the discrepancy in antitumor outcomes between in vitro and in vivo settings warrants further investigation. In our future research, we will solve this problem more intuitively by directly detecting the distribution of nanoparticles. Although the current photothermal bone cement system shows promising results in animal models, translational challenges remain due to interspecies differences. Subsequent studies should therefore incorporate human cell-based models to improve clinical relevance. Future work will focus on evaluating this strategy in surgical resection scenarios combined with CS-$Cu_{2-x}Se$+NIR therapy, quantifying related cytokine levels (eg, TNF-α, IFN-γ) via ELISA, and employing immunocompetent models to analyze immune cell infiltration (eg, macrophages, T cells, dendritic cells) for a more comprehensive understanding of the antitumor immune mechanism.

Acknowledgments

Ruitang Liu, Ruilong Sun and Yun Xue are Co-first authors. Bo Fan and Qiuming Gao are Co-corresponding authors.

Funding

This work was supported by Natural Science Foundation of Gansu Province (25JRRA809) and Gansu University of Chinese Medicine (YBXM-202415).

Disclosure

The authors report no conflicts of interest in this work.

References

1. Huang L, Wang J, Xu J, et al. Ferroptosis in osteogenic differentiation: a narrative review of bone regeneration metabolism. *Regen Med Rep*. 2025;2:100–107. doi:10.4103/REGENMED.REGENMED-D-25-00007
2. Lian H, Zhang J, Hou S, et al. Immunotherapy of osteosarcoma based on immune microenvironment modulation. *Front Immunol*. 2024;15:1498060. doi:10.3389/fimmu.2024.1498060
3. Cersosimo F, Lonardi S, Bernardini G, et al. Tumor-associated macrophages in osteosarcoma: from mechanisms to therapy. *Int J Mol Sci*. 2020;21:5207. doi:10.3390/ijms21155207
4. Biazzo A, De Paolis M. Multidisciplinary approach to osteosarcoma. *Acta Orthop Belg*. 2016;82:690–698.
5. Kansara M, Teng MW, Smyth MJ, Thomas DM. Translational biology of osteosarcoma. *Nat Rev Cancer*. 2014;14:722–735. doi:10.1038/nrc3838
6. Hu Y, Yang R, Ni S, Song Z. Bibliometric analysis of targeted immunotherapy for osteosarcoma-current knowledge, hotspots and future perspectives. *Front Immunol*. 2024;15:1485053. doi:10.3389/fimmu.2024.1485053
7. Adewuyi E, Chorya H, Muili A, et al. Chemotherapy, immunotherapy, and targeted therapy for osteosarcoma: recent advancements. *Crit Rev Oncol Hematol*. 2025;206:104575. doi:10.1016/j.critrevonc.2024.104575
8. Zhang H, Wang Y, Qiang H, et al. Exploring the frontiers: the potential and challenges of bioactive scaffolds in osteosarcoma treatment and bone regeneration. *Mater Today Bio*. 2024;29:101276. doi:10.1016/j.mtbio.2024.101276
9. Li C, Zhang W, Nie Y, et al. Time-sequential and multi-functional 3d printed MgO 2 /PLGA scaffold developed as a novel biodegradable and bioactive bone substitute for challenging postsurgical osteosarcoma treatment. *Adv Mater*. 2024;36:e2308875. doi:10.1002/adma.202308875
10. Huang B, Li G, Cao L, et al. Nanoengineered 3D-printing scaffolds prepared by metal-coordination self-assembly for hyperthermia-catalytic osteosarcoma therapy and bone regeneration. *J Colloid Interface Sci*. 2024;672:724–735. doi:10.1016/j.jcis.2024.06.055
11. Huo L, Han Z, Jiao Z, et al. Introduction of temporomandibular joint and skull base combined reconstruction by autogenous bone graft. *Clin Oral Investig*. 2023;27:2513–2520. doi:10.1007/s00784-023-05065-4
12. Kungvarnchaikul I, Subbalekha K, Sindhavajiva PR, Suwanwela J. Deproteinized bovine bone and freeze-dried bone allograft in sinus floor augmentation: a randomized controlled trial. *Clin Implant Dent Relat Res*. 2023;25:343–351. doi:10.1111/cid.13179
13. de Carvalho ABG, Rahimnejad M, Oliveira RL, et al. Personalized bioceramic grafts for craniomaxillofacial bone regeneration. *Int J Oral Sci*. 2024;16:62. doi:10.1038/s41368-024-00327-7
14. Vaishya R, Chauhan M, Vaish A. Bone cement. *J Clin Orthop Trauma*. 2013;4:157–163. doi:10.1016/j.jcot.2013.11.005
15. Lepoutre N, Meylheuc L, Bara GI, Barbé L, Bayle B. Bone cement modeling for percutaneous vertebroplasty. *J Biomed Mater Res B Appl Biomater*. 2019;107:1504–1515. doi:10.1002/jbm.b.34242

16. Xu H, Tian F, Liu Y, et al. Magnesium malate-modified calcium phosphate bone cement promotes the repair of vertebral bone defects in minipigs via regulating CGRP. *J Nanobiotechnology*. 2024;22(368). doi:10.1186/s12951-024-02595-1
17. Sandhya S, Mohanan PV, Sabareeswaran A, Varma HK, Komath M. Preclinical safety and efficacy evaluation of 'BioCaS' bioactive calcium sulfate bone cement. *Biomed Mater*. 2017;12:015022. doi:10.1088/1748-605X/aa5522
18. Ambard AJ, Mueninghoff L. Calcium phosphate cement: review of mechanical and biological properties. *J Prosthodont*. 2006;15:321–328. doi:10.1111/j.1532-849X.2006.00129.x
19. Duarte MAH, Marciano MA, Vivan RR, et al. Tricalcium silicate-based cements: properties and modifications. *Braz Oral Res*. 2018;32:e70. doi:10.1590/1807-3107bor-2018.vol32.0070
20. D'Amico G, Muwaquet Rodriguez S. Effectiveness of tricalcium silicate-based cements: systematic review and meta-analysis. *Saudi Dent J*. 2024;36:208–213. doi:10.1016/j.sdentj.2023.10.015
21. Lanzillotti C, Iaquinta MR, De Pace R, et al. Osteosarcoma cell death induced by innovative scaffolds doped with chemotherapeutics. *J Cell Physiol*. 2024;239:e31256. doi:10.1002/jcp.31256
22. Ouchi S, Niiyama E, Sugo K, et al. Shape-memory balloon offering simultaneous thermo/chemotherapies to improve anti-osteosarcoma efficacy. *Biomater Sci*. 2021;9:6957–6965. doi:10.1039/d1bm00780g
23. Kaneko TS, Sehgal V, Skinner HB, et al. Radioactive bone cement for the treatment of spinal metastases: a dosimetric analysis of simulated clinical scenarios. *Phys Med Biol*. 2012;57:4387–4401. doi:10.1088/0031-9155/57/13/4387
24. Keyak JH, Eijansantos ML, Rosecrance KG, et al. A preliminary safety assessment of vertebral augmentation with(32)P brachytherapy bone cement. *Phys Med Biol*. 2022;67:075007. doi:10.1088/1361-6560/ac5e5d
25. Rezaei B, Yari P, Sanders SM, et al. Magnetic nanoparticles: a review on synthesis, characterization, functionalization, and biomedical applications. *Small*. 2024;20:e2304848. doi:10.1002/smll.202304848
26. Yan T, Su M, Wang Z, Zhang J. Second near-infrared plasmonic nanomaterials for photoacoustic imaging and photothermal therapy. *Small*. 2023;19:e2300539. doi:10.1002/smll.202300539
27. Guo S, Gu D, Yang Y, Tian J, Chen X. Near-infrared photodynamic and photothermal co-therapy based on organic small molecular dyes. *J Nanobiotechnology*. 2023;21:348. doi:10.1186/s12951-023-02111-x
28. Xie M, Gong T, Wang Y, et al. Advancements in photothermal therapy using near-infrared light for bone tumors. *Int J Mol Sci*. 2024;25:4139. doi:10.3390/ijms25084139
29. Xu C, Ma B, Peng J, et al. Tricalcium silicate/graphene oxide bone cement with photothermal properties for tumor ablation. *J Mater Chem B*. 2019;7:2808–2818. doi:10.1039/c9tb00246d
30. Qu Y, Zhuang H, Zhang M, et al. Bone cements for therapy and regeneration for minimally invasive treatment of neoplastic bone defects. *J Mater Chem B*. 2021;9:4355–4364. doi:10.1039/d1tb00703c
31. Xia YN, Zu H, Guo H, et al. Preclinical safety and hepatotoxicity evaluation of biomineralized copper sulfide nanoagents. *J Nanobiotechnology*. 2022;20:185. doi:10.1186/s12951-022-01399-5
32. Schneider L, Kalt M, Koch S, et al. BODIPY-based photothermal agents with excellent phototoxic indices for cancer treatment. *J Am Chem Soc*. 2023;145:4534–4544. doi:10.1021/jacs.2c11650
33. Wu J, Zhang Z, Qiao C, et al. Synthesis of monodisperse ZIF-67@CuSe@PVP nanoparticles for ph-responsive drug release and photothermal therapy. 2021.
34. Zhang H, Wang T, Liu H, et al. Second near-infrared photodynamic therapy and chemotherapy of orthotopic malignant glioblastoma with ultra-small Cu 2−x Se nanoparticles. *Nanoscale*. 2019;11:7600–7608. doi:10.1039/c9nr01789e
35. Lu S, Li Y, Yu Y. Glutathione-scavenging celastrol-Cu nanoparticles induce self-amplified cuproptosis for augmented cancer immunotherapy. *Adv Mater*. 2024;36:e2404971. doi:10.1002/adma.202404971
36. Li K, Xu K, He Y, et al. Functionalized tumor-targeting nanosheets exhibiting Fe(II) overloading and GSH consumption for ferroptosis activation in liver tumor. *Small*. 2021;17:e2102046. doi:10.1002/smll.202102046
37. Kou L, Sun R, Xiao S, et al. Ambidextrous approach to disrupt redox balance in tumor cells with increased ros production and decreased GSH synthesis for cancer therapy. *ACS Appl Mater Interfaces*. 2019;11:26722–26730. doi:10.1021/acsami.9b09784
38. Matas-Rico E, Moolenaar WH. Tumor immune escape by autotaxin: keeping eosinophils at bay. *Trends Cancer*. 2024;10:283–285. doi:10.1016/j.trecan.2024.03.002
39. Cifric S, Turi M, Folino P, et al. DAMPening tumor immune escape: the role of endoplasmic reticulum chaperones in immunogenic chemotherapy. *Antioxid Redox Signal*. 2024;41:661–674. doi:10.1089/ars.2024.0558
40. Ahmadi M, Abbasi R, Rezaie J. Tumor immune escape: extracellular vesicles roles and therapeutics application. *Cell Commun Signal*. 2024;22:9. doi:10.1186/s12964-023-01370-3
41. Miao Z, Li J, Wang Y, et al. Hsa_circ_0136666 stimulates gastric cancer progression and tumor immune escape by regulating the miR-375/PRKDC axis and PD-L1 phosphorylation. *Mol Cancer*. 2023;22:205. doi:10.1186/s12943-023-01883-y
42. Wu Q, You L, Nepovimova E, et al. Hypoxia-inducible factors: master regulators of hypoxic tumor immune escape. *J Hematol Oncol*. 2022;15:77. doi:10.1186/s13045-022-01292-6
43. Zheng Y, Han Y, Wang T, et al. Reprogramming tumor-associated macrophages via ros-mediated novel mechanism of ultra-small Cu 2−x nanoparticles to enhance anti-tumor immunity. *Adv Funct Mater*. 2022;32:2108971. doi:10.1002/adfm.202108971
44. Han Y, Wang T, Liu H, et al. The release and detection of copper ions from ultrasmall theranostic Cu 2−x Se nanoparticles. *Nanoscale*. 2019;11:11819–11829. doi:10.1039/c9nr02884f
45. Wang X-M, Huang L, Wang Y-J, et al. Highly efficient near-infrared photothermal antibacterial membrane with incorporated biogenic CuSe nanoparticles. *Chem Eng J*. 2021;405:126711. doi:10.1016/j.cej.2020.126711
46. Wu J, Wu GL, Yang Q. Illuminating the future: NIR-II visualizes gas therapy for precision cancer treatment. *Med Gas Res*. 2024;14:172–174. doi:10.4103/mgr.MEDGASRES-D-23-00060
47. Zhao X, Gao J, Han H, et al. Bioactive strong biodegradable bone cement for rapid osteointegration and osteogenesis. *Chem Eng J*. 2023;474:15. doi:10.1016/j.cej.2023.145609
48. Ouyang Y, Zhang R, Zhang Q, Yan Y. Polydopamine-modified composite bone cement for cancellous bone repair: synergism of bioactivity, antibacterial properties, and biodegradability. *Biomacromolecules*. 2025;26:3538–3551. doi:10.1021/acs.biomac.5c00157

49. Ichikawa Y, Sato B, Hirano SI, Takefuji Y, Satoh F. Realizing brain therapy with "smart medicine": mechanism and case report of molecular hydrogen inhalation for Parkinson's disease. *Med Gas Res*. 2024;14:89–95. doi:10.4103/2045-9912.385949
50. Mannion J, Gifford V, Bellenie B, et al. A RIPK1-specific PROTAC degrader achieves potent antitumor activity by enhancing immunogenic cell death. *Immunity*. 2024;57:1514–1532.e1515. doi:10.1016/j.immuni.2024.04.025
51. Galassi C, Klapp V, Yamazaki T, Galluzzi L. Molecular determinants of immunogenic cell death elicited by radiation therapy. *Immunol Rev*. 2024;321:20–32. doi:10.1111/imr.13271
52. Wang C, Zhang M, Peng J, et al. Combining cisplatin with Pinellia pedatisecta Schott lipid-soluble extract induces tumor immunogenic cell death in cervical cancer. *Phytomedicine*. 2024;128:155504. doi:10.1016/j.phymed.2024.155504
53. Ding Q, Tang W, Li X, et al. Mitochondrial-targeted brequinar liposome boosted mitochondrial-related ferroptosis for promoting checkpoint blockade immunotherapy in bladder cancer. *J Control Release*. 2023;363:221–234. doi:10.1016/j.jconrel.2023.09.024
54. Liao LS, Chen Y, Hou C, et al. Potent Zinc(II)-based immunogenic cell death inducer triggered by ROS-mediated ERS and mitochondrial Ca 2+ overload. *J Med Chem*. 2023;66:10497–10509. doi:10.1021/acs.jmedchem.3c00603
55. Chen YZ, Yong MJ, Tan VY, et al. The effect of a setting accelerator on the physical and mechanical properties of a fast-set white portland cement mixed with nano-zirconium oxide. *Eur Endod J*. 2023;8:215–224. doi:10.14744/eej.2023.36449
56. Yousefi K, Manesh HD, Khalifeh AR, Gholami A. Fabrication and characterization of a nanofast cement for dental restorations. *Biomed Res Int*. 2021;2021:7343147. doi:10.1155/2021/7343147
57. Liberto T, Nenning A, Bellotto M, et al. Detecting early-stage cohesion due to calcium silicate hydration with rheology and surface force apparatus. *Langmuir*. 2022;38:14988–15000. doi:10.1021/acs.langmuir.2c02783
58. Camerini R, Poggi G, Ridi F, Baglioni P. The kinetic of calcium silicate hydrate formation from silica and calcium hydroxide nanoparticles. *J Colloid Interface Sci*. 2022;605:33–43. doi:10.1016/j.jcis.2021.06.168
59. Yang L, Zhao Z, Tian B, et al. A singular plasmonic-thermoelectric hollow nanostructure inducing apoptosis and cuproptosis for catalytic cancer therapy. *Nat Commun*. 2024;15:7499. doi:10.1038/s41467-024-51772-1
60. Liu Z-N, Yu -L-L, Liu P, et al. Overcoming the p-EMT-mediated stromal barrier at the tumor periphery with hybrid membrane-camouflaged nanoplatform for enhanced chemotherapy. *Nano Today*. 2025;65:102877. doi:10.1016/j.nantod.2025.102877
61. Liu JY, Liu XH, Zhong NN, et al. Barriers in bone tumor treatment: the emerging role of drug delivery systems. *Med Oncol*. 2025;42:294. doi:10.1007/s12032-025-02853-8
62. Xie Y, Shi Y, Li Z, et al. NIR-programmed trimodal macrophage nanovectors for effective anti-tumor therapy in mice model. *Int J Nanomed*. 2025;20:11295–11314. doi:10.2147/ijn.S542647